Earthquake Delay and Rupture Velocity in Near-Field Dynamic Triggering Dictated by Stress-Controlled Nucleation

Peng Dong[†1,2], Rong Chen[†3], Kaiwen Xia[*1,2], Wei Yao[4], Zhigang Peng[5], and Derek Elsworth[6]

Abstract

Dynamic triggering of earthquakes by seismic waves generated by another earthquake is widely observed, while the underlying nucleation mechanisms remain unclear. We report here dynamically triggered earthquakes on laboratory faults with tightly constrained imaging of the triggering process. The arriving stress wave alters the contact state of the laboratory fault and initiates rupture nucleation in two distinct phases. The triggered rupture grows at a fraction of the shear-wave velocity ($\sim 0.4C_S$) and then transits to a very slow velocity ($\sim 0.1C_S$) before culminating into runaway shear. This intervening very slow rupture phase is present only for seismic ratios conducive to sub-Rayleigh ruptures and is notably absent for supershear events. Thus, the delay in triggering decreases to a minimum for triggered supershear ruptures, whereas it scales with the stress state for triggered sub-Rayleigh ruptures. These results may help explain key characteristics of delayed near-field dynamic triggering and provide a simple theoretical framework for dynamic triggering at greater distances.

Cite this article as Dong, P., R. Chen, K. Xia, W. Yao, Z. Peng, and D. Elsworth (2022). Earthquake Delay and Rupture Velocity in Near-Field Dynamic Triggering Dictated by Stress-Controlled Nucleation, *Seismol. Res. Lett.* **XX**, 1–12, doi: 10.1785/0220220264.

Supplemental Material

Introduction

Earthquakes can trigger other seismic events both locally and thousands of kilometers apart (Kilb *et al.*, 2000; Gomberg *et al.*, 2003; West *et al.*, 2005; Felzer and Brodsky, 2006; Hill and Prejean, 2015). Near-field triggering generally refers to earthquakes being triggered within a few fault lengths from the mainshock (Harris, 1998; Freed, 2005), which has been attributed to static or dynamic stress changes (Felzer and Brodsky, 2006; Richards-Dinger *et al.*, 2010; van der Elst and Brodsky, 2010). One unique feature of near-field dynamic triggering is the time delay between the triggering stress-wave arrival and the onset of the resulting triggered event (Hill and Prejean, 2015). The time delay ranges from tens of seconds to years, which is either consistent with slow rupture propagation or implies a delayed triggering case (Hudnut *et al.*, 1989; Belardinelli *et al.*, 1999; Antonioli *et al.*, 2002, 2006; Nissen *et al.*, 2016). Understanding the key mechanisms of dynamic triggering of earthquakes, controls on this time delay, and modes of the resulting event have important implications in defining seismic hazards and precursors (Brink *et al.*, 2020).

In the theoretical framework of Coulomb friction, faulting occurs when the shear stress acting on the fault exceeds its frictional strength. Therefore, dynamic triggering occurs when the dynamic stress carried by the seismic waves brings the shear stress beyond the strength of the fault (Hill and Prejean, 2015). However, extended time delays are generally inconsistent with Coulomb failure models because such models imply nearly instantaneous triggering. Thus, time delays are usually attributed to additional physical processes that invoke a time-dependent acceleration, including triggered aseismic slip (Shelly *et al.*, 2011; Blank *et al.*, 2021), alteration of frictional contact of fault (Johnson and Jia, 2005; Parsons, 2005; Johnson *et al.*, 2008), and triggered time-dependent increase in pore pressure (Brodsky *et al.*, 2003; Freed, 2005). In addition, for a fault controlled by the rate and state-dependent friction, delayed triggering is also theoretically possible (Gomberg *et al.*, 1997; Perfettini *et al.*, 2003). However, it is difficult to provide direct experimental evidence to verify these postulates. Recently, van der Elst and Savage (van der Elst and Savage, 2015) have shown that the basic rate and state-dependent friction could reproduce

1. Institute of Geosafety, School of Engineering and Technology, China University of Geosciences (Beijing), Beijing, China, https://orcid.org/0000-0002-8121-7732 (PD); https://orcid.org/0000-0001-8609-608X (KX); 2. Department of Civil and Mineral Engineering, University of Toronto, Toronto, Ontario, Canada; 3. College of Science, National University of Defense Technology, Changsha, China, https://orcid.org/0000-0003-1566-9359 (RC); 4. State Key Laboratory of Hydraulic Engineering Simulation and Safety, School of Civil Engineering, Tianjin University, Tianjin, China; 5. School of Earth and Atmospheric Sciences, Georgia Institute of Technology, Atlanta, Georgia , U.S.A., https://orcid.org/0000-0002-0019-9860 (ZP); 6. Energy and Mineral Engineering & Geosciences, G3 Center and EMS Energy Institute, Pennsylvania State University, University Park, Pennsylvania, U.S.A., https://orcid.org/0000-0002-4942-1151 (DE)

*Corresponding author: kaiwen.xia@utoronto.ca

†These authors equally contributed to this work.

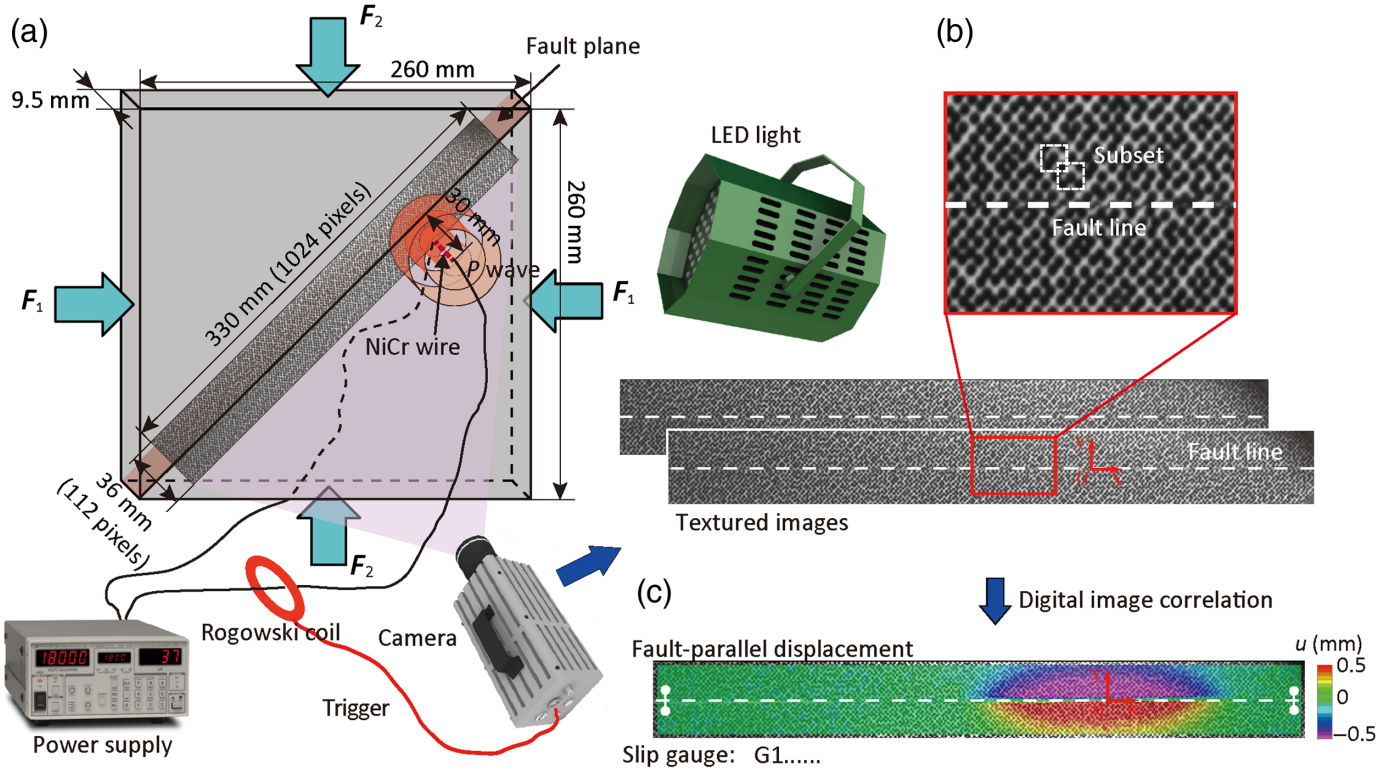

Figure 1. Schematics of the experimental setup and diagnostic methods for the earthquake dynamic triggering of earthquake experiments. (a) The experimental setup consists of the biaxial-loading fault model made of polymethyl methacrylate (PMMA; shear-wave velocity $C_S = 1.21$ km/s and longitudinal wave velocity $C_P = 2.74$ km/s), the light-emitting diode (LED) light, the high-speed camera, and the exploding wire system. A rectangular region (field of view) enclosing the fault is textured with speckle patterns. (b) The images of the field of view taken by the high-speed camera. (c) Displacement field near the fault obtained using the digital image correlation (DIC) method. A number of (virtual) digital slip gauges are arranged along the fault line to detect the evolution of the slip distribution as detailed in the supplemental material. The color version of this figure is available only in the electronic edition.

delayed triggering of earthquakes. However, their theoretical predictions do not match well with their experimental results.

Over the past few decades, laboratory experiments have significantly extended our understanding of earthquake physics, especially on the nucleation process, rupture dynamics, and friction evolution (Rubino *et al.*, 2017, 2020; Svetlizky *et al.*, 2017; Tal *et al.*, 2022). For example, the slow nucleation phase preceding dynamic ruptures is widely observed in stick-slip experiments (Ohnaka and Kuwahara, 1990; Nielsen *et al.*, 2010; Latour *et al.*, 2013; McLaskey, 2019), which is regarded as a precursor to earthquakes. In addition, with an elaborate diagnostic method, Rubinstein *et al.* (2004, 2007) revealed that it is the slow detachment front that weakens the fault and leads to the final failure when it traverses the fault. Regarding rupture dynamics, Xia *et al.* (2004) showed that an expanding sub-Rayleigh rupture can jump into the supershear regime through the Burridge–Andrews mechanism. In addition, spontaneously nucleated supershear ruptures have also been confirmed in other experiments (Ben-David *et al.*, 2010; Passelègue *et al.*, 2013). However, these experimental studies are mainly concentrated on the spontaneously nucleated earthquakes, where the ruptures initiate as a result of quasi-statically building-up stress (Ohnaka and Kuwahara, 1990; Rubinstein *et al.*, 2004) or local release of normal stress (Xia *et al.*, 2004; Rubino *et al.*, 2017). The detailed nucleation process and rupture dynamics for dynamically triggered events have not yet been experimentally observed.

The objective of this work is to understand the time delay phenomenon of near-field dynamic triggering. We perform highly constrained experiments to reveal the entire process of near-field dynamic triggering from nucleation to dynamic propagation. Using P wave induced by an exploding wire, we disturb faults preloaded to various levels, leading to rupture nucleation and subsequent fully dynamic propagation. The widely observed time delay in dynamic triggering from field studies is reproduced in the laboratory and is recognized as the duration for rupture nucleation after the stress-wave perturbation. Our results suggest that the earthquake triggering mechanism is the alternation of fault contact in combination with the disturbed rupture nucleation.

Methods

Experimental design

We seek to understand the physical processes that control the time delay and subsequent selection of dynamic rupture velocity of earthquakes by observing triggered slip along frictionally

immobilized interfaces (i.e., the fault plane in Fig. 1). We eliminate any influence of fluid flow and enable a tight visual constraint by adopting dry laboratory faults of polymethyl methacrylate (PMMA). In 2D problems, both *P* and *S* waves are possible triggering agents. To isolate mechanisms other than dynamic changes in the Coulomb stress, we apply purely *P*-wave triggering generated by an exploding wire (Fig. 1).

The strain magnitude of the triggering *P* wave in our experiments (order of 10^{-4} as shown in Fig. S1 and Text S1 in supplemental material available to this article) matches that for in situ near-field triggering (van der Elst and Brodsky, 2010), limiting the relevance of our experiments to near-field triggering of earthquakes only. In this study, our laboratory fault is loaded to a spectrum of stress conditions and is subjected to a uniform triggering disturbance (fixed charging voltage of 1.3 kV and fixed off-fault location).

Fault model

Our laboratory fault (Fig. 1a) transects a biaxially stressed square sheet of PMMA (density $\rho = 1200$ kg/m^3, Young's modulus E = 4.82 GPa, shear modulus $\mu = 1.73$ Gpa, Poisson's ratio $\nu = 0.40$) at 45°. The fault surfaces are carefully polished (number 600 grit sandpaper) to a uniform roughness to allow for repeatable conditions on the fault.

The laboratory fault (Fig. 1) is symmetrically disposed to distributed biaxial loads in the horizontal (F_1) and vertical (F_2) directions, resulting in the nominal normal σ_n and the shear τ_0 stresses on the fault as

$$\sigma_n = \frac{\sqrt{2}}{2}\frac{F_1 + F_2}{A}, \tau_0 = \frac{\sqrt{2}}{2}\frac{F_1 - F_2}{A}, \quad (1)$$

in which A is the contact area of the fault.

Loading conditions on the fault are defined by the nondimensional seismic ratio S as (Andrews, 1985)

$$S = \frac{\tau_s - \tau_0}{\tau_0 - \tau_d}, \quad (2)$$

in which τ_0, $\tau_s = \mu_s\sigma_n$, and $\tau_d = \mu_d\sigma_n$ are the resolved shear stress on the fault, the static frictional strength, and the dynamic strength of the fault, respectively. The static coefficient of friction μ_s is set to be 0.6. However, the dynamic coefficient of friction μ_d may be slip rate dependent (Rubino *et al.*, 2017). Here, we assume that μ_d is in the range of 0.25∼0.35 without loss of generality. To ensure the repeatability of the dimension of the specimen and the fault roughness, the specimen is reused by refreshing the fault surface with the same sandpaper every time prior to a new test.

Exploding wire technique for stress-wave disturbance

The *P*-wave triggering disturbance is induced using an off-fault exploding wire (Fig. 1). Such triggering has been extensively employed in laboratory earthquake experiments (Xia *et al.*, 2004, 2005). However, unlike existing studies in which the thin (diameter ∼0.1 mm) metal wire is buried directly inside the fault, a small hole is drilled in the plate ∼30 mm orthogonal from the fault to house the wire. A switch discharges an electrical capacitor (100 μF with voltage up to 5 kV) and generates a high current (several thousand amperes) in the thin metal wire for a short duration as measured using the Rogowski coil. The high current transforms the metal wire into a high-pressure and high-temperature plasma in less than 10 μs. The expansion of the plasma generates a pressure wave that propagates into the PMMA plate and then onto the fault. A threshold voltage of ∼600 V is required to vaporize the ∼0.08 mm diameter and ∼10 mm long nickel wire used in this study.

Because the hole hosting the wire is very small, the stress induced by the explosion is essentially compressive (Xia *et al.*, 2004), which is also verified by the explosion-induced strain field shown in Figure S1. The compressive *P* wave contributes insignificantly (or even negatively) to the Coulomb stress changes on fault segments that are close to the *P* wave source. The length of the resulting strain pulse is ∼40 mm, with a 20 mm compressive phase with the magnitude of ∼200 με and a 20 mm tensile phase with nearly zero strain.

Diagnostic imaging

A Photron FASTCAM SA1.1 high-speed camera captures images at 50,000 frames/s of the textured field of view that encloses the fault (Fig. 1). The field of view at this frame rate is 1024 × 112 pixels, corresponding to a physical field of view of 330 × 36 mm. The camera is triggered by the ignition signal of the exploding wire through the Rogowski coil.

Digital image correlation (DIC) quantitatively recovers the dynamic displacement field during a laboratory earthquake rupture. This technique has been successfully used in recent laboratory earthquake experiments (Rubino *et al.*, 2017, 2020; Zhuo *et al.*, 2018). We print a random speckle of monodispersed black dots on the surface of the PMMA sheet orthogonal to the plane of the laboratory fault. This locates the traversing rupture pulse with the best correlation result returned when each dot encloses about three pixels in the screen grab (Chen *et al.*, 2015). DIC analyses are conducted using the commercial correlation software VIC-2D (Correlation Solutions Inc.) and the "Fill-Boundary" algorithm. This algorithm is optimized to recover shear offsets across a displacement discontinuity. For the calculation, the size of the subset is chosen as 15 × 15 pixels with a step of three pixels. The same set of DIC analysis parameters is used to calculate the displacement field for all experiments.

The measurement accuracy is affected by many factors, such as the speckle pattern, imaging resolution, camera self-noise, lightning variations, and DIC analysis parameters. To evaluate the performance of the diagnostic system for displacement measurements, we conduct the error analysis following the existing study (Rubino *et al.*, 2019). Using the diagnostic system, we

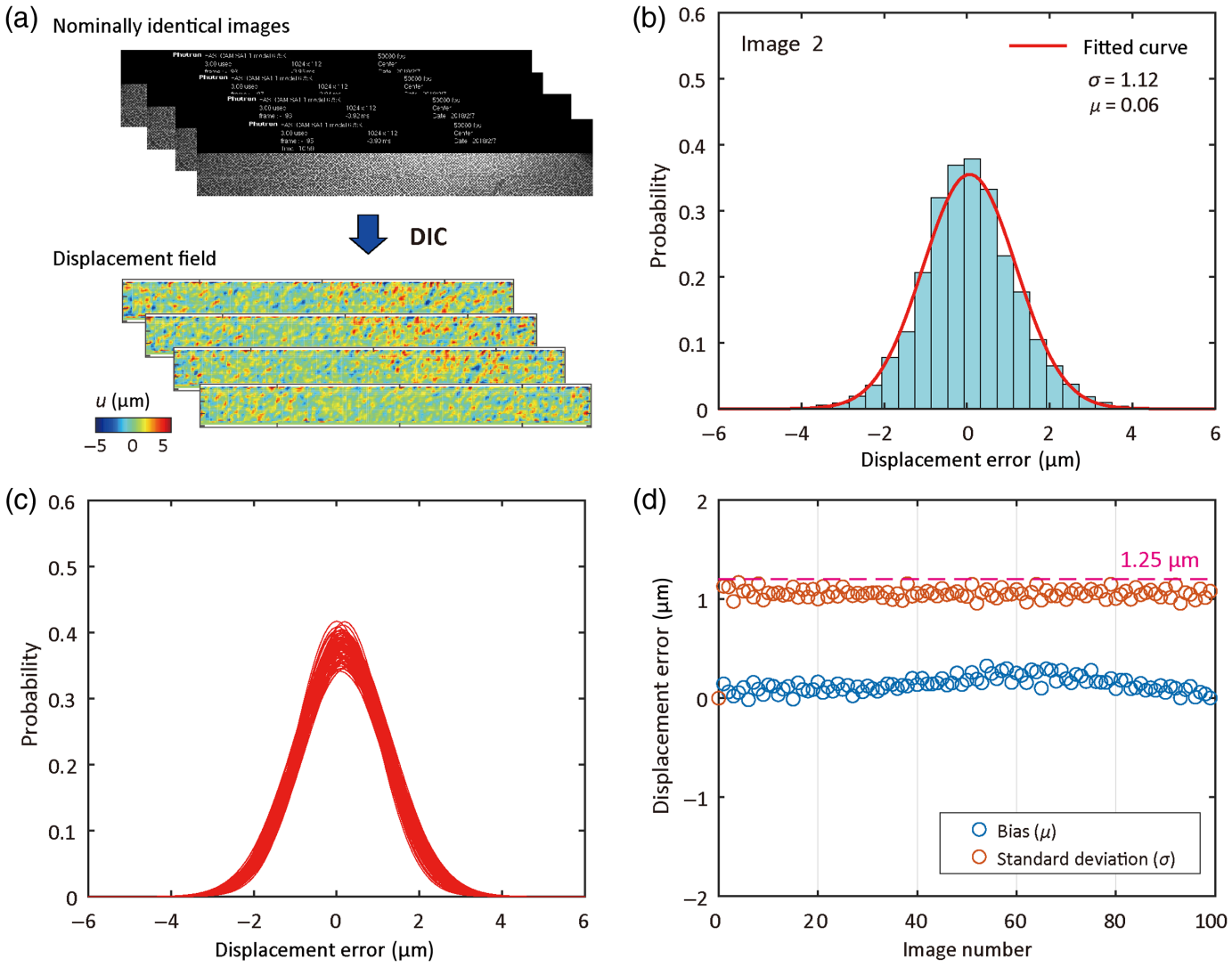

Figure 2. Error analysis for the displacement measurements. (a) The displacement field of the nominally identical images produced by the diagnostic system. The nominally identical images refer to the sequence of images of the static sample. (b) Probability distribution of the displacement error for the second image as an example. The normal distribution function is used to fit the distribution probability. (c) The fitted normal distribution function for a sequence of images. (d) The bias and the standard deviation for each image. The color version of this figure is available only in the electronic edition.

obtain the displacement field for a sequence of one hundred images of the static sample (Fig. 2a). Because these images are nominally identical, the resulting displacement can be considered to be the error with the diagnostic system. It can be seen that the displacement error generally follows a normal distribution (Fig. 2b). Therefore, we use the normal distribution function to fit the probability distribution of the displacement error for each image (Fig. 2c). The fitted bias and standard deviation for each image are shown in Figure 2d. The standard deviation is less than 1.25 μm, and the bias is nearly zero. Such a deviation is identified as the measurement error of the diagnostic system, which is equivalent to 0.004 pixels. The accuracy of the displacement measurement is reasonable and meets the measurement requirement of this work.

Results

Nucleation processes in triggered sub-Rayleigh and supershear rupture events

Typical results for a triggered sub-Rayleigh (the final rupture velocity below the Rayleigh-wave velocity of the material) event and a triggered supershear event are presented in Figure 3. Time zero is set from the known ignition timing from the Rogowski coil (Fig. 1). The stress-wave disturbance reaches the fault at about 11 μs($= 30$ mm$/C_P$). The perturbation stress-wave decays rapidly with distances, and thus, the strongest perturbation is expected on the fault segments closest to E′, the orthogonal projection of the explosion site onto the fault (see Fig. S1). We locate the rupture tip using the spatiotemporal distribution of the fault slip (Fig. 3 and Text S2 and Fig. S2).

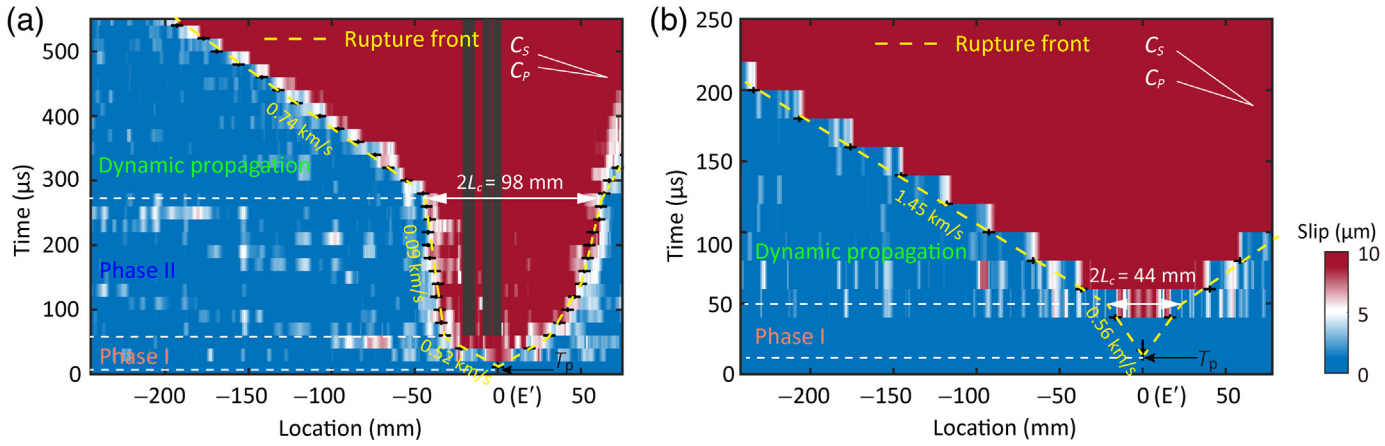

Figure 3. Rupture processes of a representative triggered (a) sub-Rayleigh and (b) supershear events. The spatiotemporal evolution of fault slip is used to track the rupture fronts (yellow dashed lines). The black stripes in panel (a) are due to the debonding of the speckle pattern at three patches, which does not affect our tracking of the rupture front. The stress-wave disturbance first arrives on the fault at E′ (location = 0 mm) at the projection of the explosion site (E) (see Fig. S1) and at an arrival time (T_P) of 11 μs relative to the exploding of the wire. The color version of this figure is available only in the electronic edition.

The dynamic rupture velocity of the triggered events depends on the loading condition as dictated by the distributed boundary loads F_1 and F_2 (Fig. 1) and features two characteristic nucleation processes. We explore the essential characteristics for separate events featuring sub-Rayleigh and supershear ruptures in shown Figure 3 and discussed in the following.

Sub-Rayleigh rupture. The nucleation process for a sub-Rayleigh event is illustrated in Figure 3a. The seismic ratio S is 0.68 for this event. Initially, the rupture expands bilaterally from E′ after the stress-wave arrival and with an average velocity of ~520 m/s (~0.41C_S). We term this stage phase I. The slight asymmetry of rupture growth is explained by edge effects from the proximity of the right-side loading platen (Fig. 1). Then at ~56 μs, the nucleation evolves into phase II, characterized by a reduced rupture velocity of ~90 m/s. This velocity is slightly higher than the rupture velocity (30–50 m/s) observed during the nucleation process of spontaneous rupture (Nielsen *et al.*, 2010), which finally evolves into dynamic propagation by slowly increasing the quasistatic boundary loads only. The small difference in the rupture velocity may be attributed to the dynamic nature of the stress-wave disturbance because the loading rate of the stress-wave is higher than that of the quasistatic loads in spontaneous rupture tests and the rupture growth velocity within the nucleation zone is rate dependent (Kato *et al.*, 1992; Ohnaka, 1996; Kaneko *et al.*, 2016). Because there is no remarkable acceleration in rupture speed during this stage, phase II resembles quasistatic, stable growth observed for spontaneous ruptures (Ohnaka, 1996; Nielsen *et al.*, 2010; Latour *et al.*, 2013). At about 275 μs, the rupture attains a critical, theoretical unstable length ($2L_c$) of 98 mm, after which there is a transient but rapid acceleration in rupture speed. Finally, the dynamic rupture attains a velocity of 740 m/s (~0.61C_S). Thus, the time delay for this sub-Rayleigh event is determined as 264 μs by subtracting the stress-wave propagation delay (11 μs) from the timing of the onset of rupture acceleration (275 μs). Such an observation of rupture velocity variation is similar to that reported previously (Rubinstein *et al.*, 2007), although the loading conditions are quite different.

Supershear Rupture. For the triggered supershear event, the seismic ratio S is 0.68. For this event, the fully dynamic rupture begins at 50 μs (Fig. 3b) and with a higher rupture velocity of 1.45 km/s–representative of supershear (~1.20C_S). Furthermore, the critical rupture length ($2L_c$) is smaller at ~44 mm (vs. ~62 mm sub-Rayleigh), and the time delay is shorter (~39 vs. ~54 μs). The nucleation process prior to the dynamic rupture is not well constrained due to the limited resolution. However, during nucleation, the average rupture velocity can be estimated at ~560 m/s from Figure 3b, which is consistent with the velocity during phase I, as observed in Figure 3a. Thus, we identify only phase I behavior during the nucleation of this supershear event, with phase II being absent. In addition, as compared with the spontaneous rupture nucleation, the acceleration phase immediately prior to the dynamic rupture propagation is too transient to be discerned, perhaps due to the fact that the supershear transition is very fast. This direct supershear transition has been reported for sufficiently stressed faults in numerical simulations (Liu *et al.*, 2014).

Combined rupture behaviors. A total of eight earthquake dynamic triggering experiments are conducted to probe the general rupture behaviors of the triggered events. To better understand the nucleation process of triggered events, we summarize the experimental results in Figure 4. The events are approximately symmetrical, but we show only the time delays for the left-propagating events with the longer rupture length (60 mm), avoiding the boundary influence of the right loading

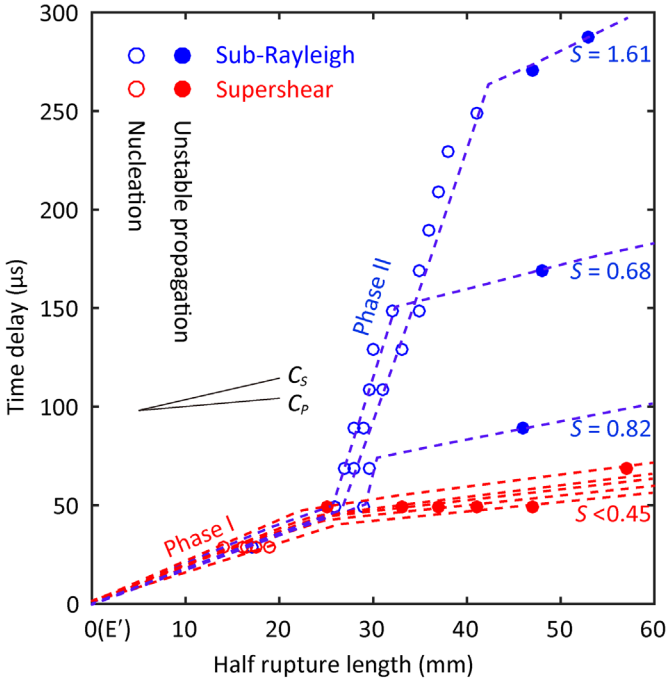

Figure 4. Compilation of observations from all tests with rupture fronts in space–time view. Dashed polylines correspond to the rupture front of triggered events on the left branch of the fault (to 60 mm). Cycles indicate the location of rupture tips for each event at different moments during and after the nucleation. Stress state quantified as seismic ratio S is labeled beneath the rupture fronts. The color version of this figure is available only in the electronic edition.

platen. The stacked results show that, during the nucleation process (indicated as open circles), all events exhibit similar characteristics: after initiating from E′, the rupture enters the aforementioned two phases (I & II). Depending on the static biaxial stress state, the rupture may accelerate into supershear velocity directly from phase I (with a smaller critical half rupture length L_c and absent phase II) or transit via a protracted nucleation stage to sub-Rayleigh velocity directly following phase II (with a larger L_c). There may be a critical half rupture length of ~25 mm beyond which the nucleated rupture assumes a sub-Rayleigh velocity.

Rupture velocity of dynamically triggered events

Figure 5a shows that the final rupture velocity generally decreases with increases in seismic ratio S. Supershear ruptures generally occur on weak faults (in our experiments for S <0.5), whereas sub-Rayleigh ruptures occur on strong faults (S >0.5), with an apparent time delay threshold of 50 μs. Our results highlight that the rupture speed of the triggered event can exceed the shear wavespeed, which may produce surprisingly large ground motions due to the passing of the Mach cone (Das, 2007). However, the critical value ($S \sim 0.5$) for supershear mode is significantly smaller than the threshold values of 1.77 predicted for unbounded 2D faults (Andrews, 1985) and 1.19 for 3D faults (Dunham, 2007). This smaller critical S value for triggered supershear rupture indicates that triggered supershear ruptures require more demanding stress conditions. Importantly, our observation is consistent with the results in which the spontaneous nucleated ruptures propagate at various speeds below Rayleigh wavespeeds or above the shear wavespeed (Kammer *et al.*, 2018).

Figure 5a also shows that the time delay is coupled with the seismic ratio S and rupture velocity. In Figure 5b, we explicitly display the relationship between the time delay and S. For the triggered sub-Rayleigh events, the time delay generally increases with S. Nevertheless, the time delay of the triggered supershear events seems to be independent of the seismic ratio S within the measurement error of this study. To our best knowledge, there are two likely cases of triggered supershear events: the 2001 M_w 7.8 Kunlun and the 2002 M_w 7.8 Denali fault earthquakes (Ozacar *et al.*, 2003; Ozacar and Beck, 2004). For both events, ruptures started at a nearby fault as a sub-Rayleigh subevent and then jumped to the neighboring strike-slip fault as a supershear rupture.

Discussion

Alteration of critical slip distance

Change in the mean critical slip distance d_c from dynamic disturbance has also been suggested as a mechanism for the time delay (Parsons, 2005). Similarly, in this work, it is possible for the perturbing P wave to alter the critical slip distance. Therefore, we attempt to estimate the critical slip distance d_c, based on the observed critical half rupture length L_c and the static stress states in the following using all our tests listed in Table 1.

Within the theoretical framework of slip-weakening behavior (Palmer and Rice, 1973), the critical half rupture length of the fault is (Andrews, 1976)

$$L_c = \frac{1+\nu}{\pi}\frac{(\tau_s-\tau_d)}{(\tau_0-\tau_d)^2}\mu d_c, \tag{3}$$

in which μ is the shear modulus, ν is Poisson's ratio, and d_c is the critical slip distance. τ_0, $\tau_s = \mu_s\sigma_n$, and $\tau_d = \mu_d\sigma_n$ are the resolved shear stress on the fault, the static frictional strength, and the dynamic strength of the fault, respectively. It should be noted that equation (3) is appropriate for the quasistatic nucleation process rather than the disturbed nucleation associated with dynamic process in this study because the energy release rate of dynamic ruptures is different from that of quasistatic ruptures.

To quantify the energy release rate during the disturbed nucleation process more precisely, we take the effect of rupture velocity (V_r) into consideration by introducing the velocity factor $g(V_r)$ into the available energy release rate $G(V_r)$. The available energy release rate is then

$$G(V_r) = g(V_r)\,G(0), \tag{4}$$

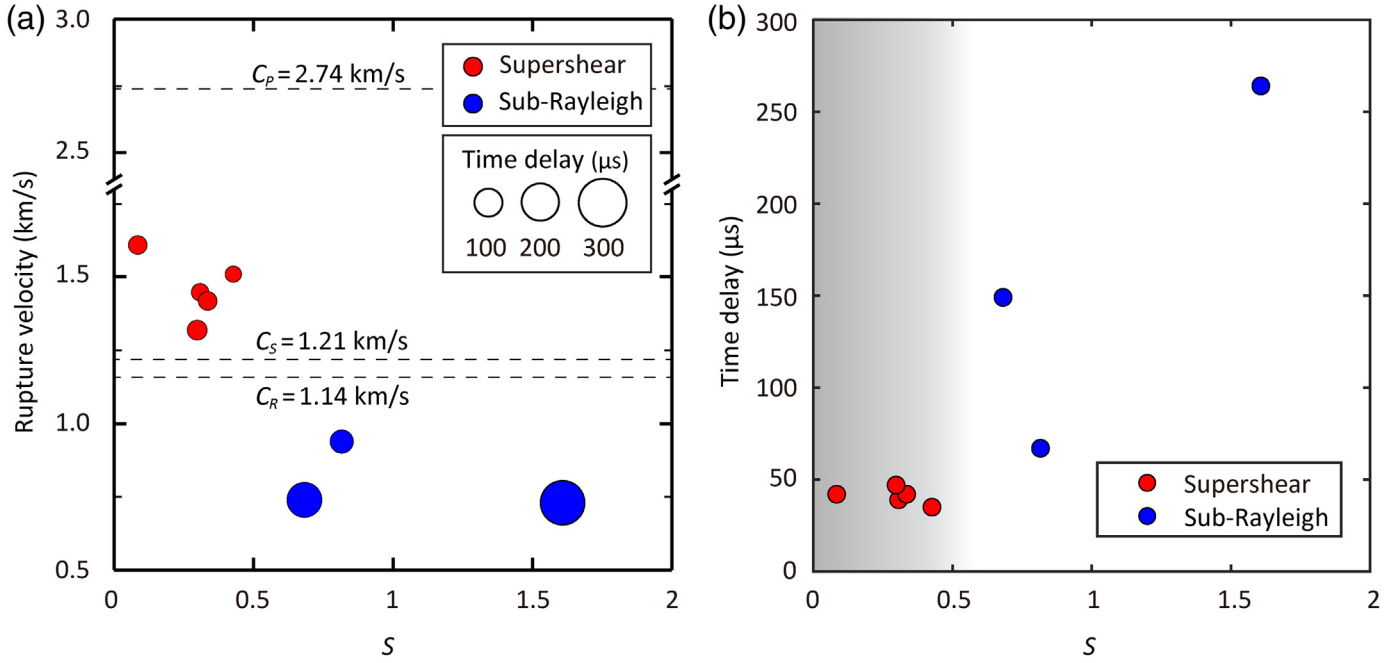

Figure 5. Rupture behaviors of triggered events. (a) Final rupture velocity of triggered events as a function of stress state that is quantified as seismic ratio S. Events complete nucleation and propagate in either sub-Rayleigh or supershear modes. Circle sizes define the time delay. (b) Dependence of time delay on the seismic ratio S. The color version of this figure is available only in the electronic edition.

in which $G(0) = \frac{\pi}{(1+\nu)\mu}(\tau_0 - \tau_d)^2 L_c$ is the available energy release rate for a critical static crack (Andrews, 1976) and $g(V_r) = (1 - V_r/C_R)/\sqrt{1 - V_r/C_S}$ is a universal function of rupture speed V_r (Fossum and Freund, 1975; Venkataraman and Kanamori, 2004). Then, at the critical half rupture length L_c, the balance between the available energy release rate with the fracture energy G_c yields

$$G(V_r) = 2G_c, \tag{5}$$

in which $G_c = 1/2(\tau_s - \tau_d)d_c$. Therefore, the critical half rupture length is then

$$L_c = \frac{1}{g(V_r)}\frac{1+\nu}{\pi}\frac{(\tau_s - \tau_d)}{(\tau_0 - \tau_d)^2}\mu d_c. \tag{6}$$

In our experiments, the dynamic rupture commences after the full passage of the stress wave from the nucleation zone. Therefore, the energy balance at the critical state (equation 6) is modestly reserved.

From equation (6), the critical slip distance for our laboratory fault is less than 10 μm based on data fitting for events

TABLE 1
Summary of Testing Conditions and Results

Test Number	Horizontal Loading, F_1 (kN)	Vertical Loading, F_2 (kN)	Normal Stress (MPa)	Shear Stress (MPa)	Seismic Ratio, S	Rupture Velocity (km/s)	Critical Rupture Length, $2L_c$ (mm)	Delay (μs)
1	34.28	9.20	8.78	5.06	0.08	1.61	40	42
2	20.49	6.64	5.48	2.80	0.43	1.51	35	35
3	10.02	3.08	2.65	1.40	0.31	1.45	44	39
4	15.72	4.90	4.16	2.18	0.33	1.42	42	42
5	8.38	2.57	2.21	1.17	0.30	1.32	43	47
6	5.89	2.15	1.62	0.75	0.82	0.94	62	67
7	6.81	2.82	1.94	0.81	1.61	0.73	98	264
8	3.59	1.26	0.98	0.47	0.68	0.74	70	149

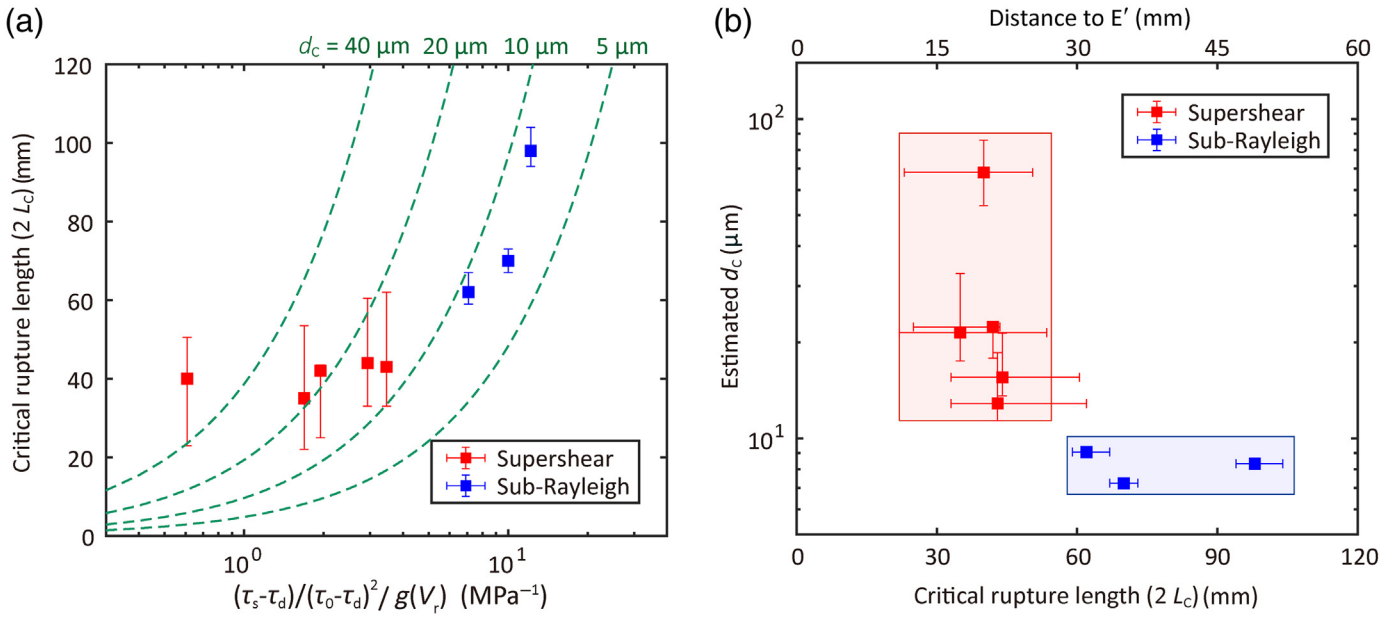

Figure 6. (a) Dependence of the critical rupture length ($2L_c$) on the stress state and nucleation dynamics. The green dashed curves correspond to theoretical predictions of the critical rupture length ($2L_c$) based on the revised model using d_c of 5, 10, 20, and 40 μm, respectively. (b) Estimated d_c as a function of the critical rupture length. The color version of this figure is available only in the electronic edition.

with critical rupture lengths ($2L_c$) larger than 50 mm (Fig. 6a). This critical slip distance d_c is similar to that estimated in earlier laboratory studies (Xia *et al.*, 2004; Svetlizky *et al.*, 2020). For events with critical rupture lengths smaller than 50 mm, the critical slip distance d_c is in the range of 10–60 μm (Fig. 6a). Comparing the estimated d_c for these events, we find that d_c of the events with critical rupture lengths $2L_c < 50$ mm is larger than that of the events with critical rupture lengths $2L_c > 50$ mm (Fig. 6b). Because the half critical rupture length (L_c) is equal to the distance between the rupture initiation point (point E′) and the rupture tips, the variation of d_c with L_c indicates the nonuniformly distributed d_c. It is clear that the fault segment close to point E′ is characterized with a larger d_c. Considering that d_c is nominally uniform on the fault before the *P*-wave perturbation, we could conclude that the perturbing *P* wave may alter the distribution of d_c.

Possible changes in fault contact state

In Figure 7, we plot the estimated d_c as a function of the distance relative to the rupture initiation point (point E′) along the fault. According to the distribution of d_c, we divide the fault into undisturbed and disturbed zones. Considering the distribution of d_c and the geometrical attenuation of the exploding wave, it is reasonable to accept that the contact state in the disturbed zone is altered by the perturbing *P* wave. As suggested by (Scholz, 1988; Harbord *et al.*, 2017), the contact state of the fault is related to the critical slip distance d_c, a frictional parameter that can be considered to be the maximum distance between asperities. Now, we are wondering how the perturbing *P* wave alters the local microscopic contact state of the fault and leads to the nonuniformly distributed d_c. However, due to the limited spatiotemporal resolution of observation of this work, we are unable to directly observe the changes in the microscopic contact state at the nucleation onset.

Supported by the quantitative results of d_c, we propose a possible explanation for the *P*-wave induced alteration of d_c. As illustrated in the bottom schematic diagrams in Figure 7, it is likely that some asperities in the disturbed zone undergo failure or damage when a perturbing *P* wave strikes the fault plane. The failure of these asperities potentially results in increased separation between active contacts and, thus, an increased d_c (Ohnaka, 2003; Harbord *et al.*, 2017). Further, this failure of microscopic asperities affects the rupture process in two ways. On the one hand, the failure of asperities changes the contact state in the disturbed zone. On the other hand, the failure of asperities may also lead to the weakening of the fault strength, which may immediately lead to the onset of rupture growth with sub-Rayleigh velocity (disturbed growth). Such a modification of contacts by seismic waves was suggested as a possible mechanism for earthquake dynamic triggering (Kilb *et al.*, 2000).

However, previous studies have shown that the population of asperities in contact would increase with static normal load, which may be due to the indentation yielding of contacts (Dieterich and Kilgore, 1994). According to this rule, it is plausible that a superposition of dynamic stress would strengthen the fault rather than trigger ruptures, which is contrary to our experimental results and speculation. However, it is not clear whether the earlier rule derived from static experiments still

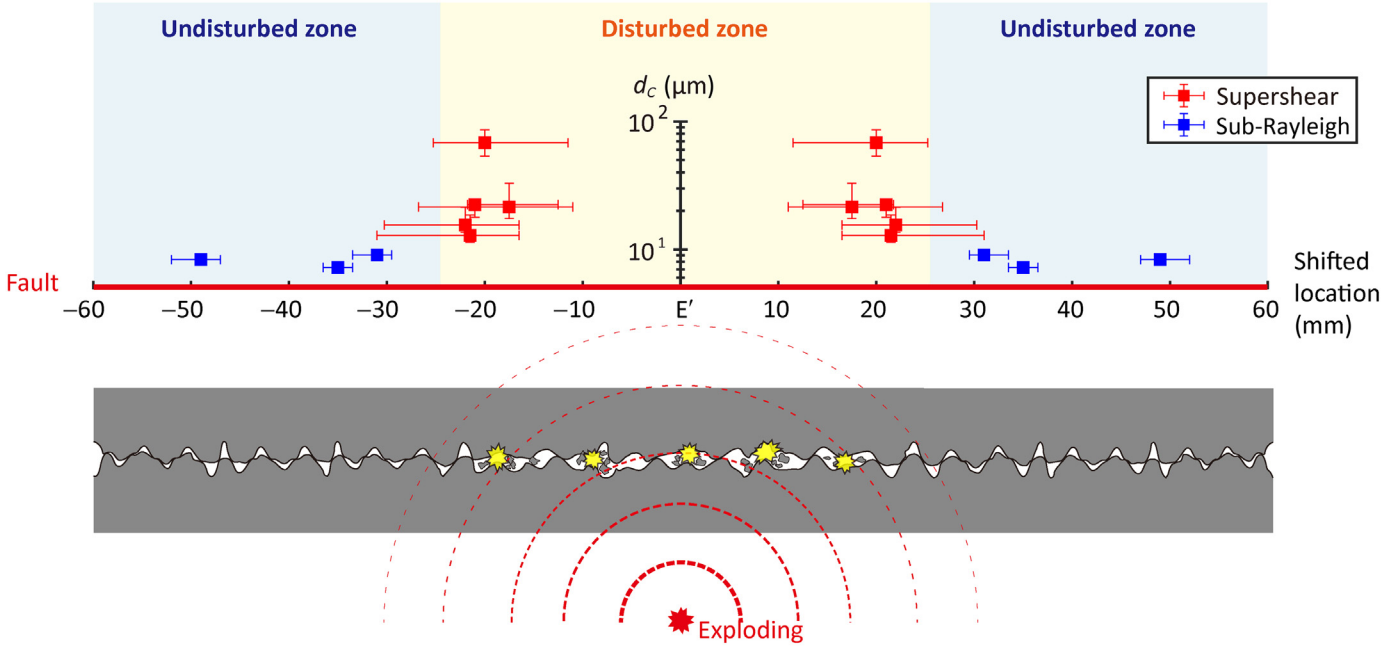

holds for this work, in which the static normal stress is superposed by a dynamic *P*-wave perturbation. It is likely that the contacts are brittle when subjected to dynamic perturbation, so the contact may undergo brittle failure. Furthermore, if the contact area increases after the passage of the *P* wave, the fault strength should increase, and there would not be triggered ruptures, which is contrary to the experimental results. Because the microscopic process responsible for the initiation of dynamic triggering has not been thoroughly resolved in this work, more efforts should be made in the future.

Figure 7. Inferred physical process leading to the change in fault contact. (Top) Distribution of d_c as a function of the distance relative to the rupture initiation point (point E′) along the fault. Depending on the distribution of d_c, two distinct zones are identified along the fault: a "disturbed zone" shaded in light yellow and an "undisturbed zone" shaded in light blue. (Bottom) Schematic diagram of the possible physical process responsible for the changes in the contact state of the fault after the passage of the perturbing *P* wave. The color version of this figure is available only in the electronic edition.

Disturbed nucleation model explaining the time delay and rupture dynamics

Because the boundary between the disturbed and undisturbed zone roughly matches the boundary between nucleation phases I and II, we term phase I in Figure 4 as "disturbed growth" and phase II as "quasistatic growth". The latter follows the term used for spontaneous rupture nucleation (Ohnaka, 1996; Latour *et al.*, 2013). As shown in Figure 8, the disturbed nucleation process is delineated by the nucleation data points for all events. Hence, for given fault roughness and triggering stress wave, the rupture nucleation and dynamic propagation are determined by the biaxial loading through the critical half rupture length L_c: the final dynamic rupture velocity is supershear if the critical half rupture length L_c is within the disturbed zone of 25 mm; otherwise, it is sub-Rayleigh.

Depending on the static loading condition, the disturbed sub-Rayleigh rupture (phase I) may directly transform into supershear within the disturbed zone or evolve into a prolonged slow quasistatic rupture (phase II), followed by a sub-Rayleigh rupture. Thus, our results reveal that, in our laboratory setting, the earthquake triggering mechanism is the alternation of fault contact in combination with the disturbed rupture nucleation. The time delay of dynamic triggering may arise from the period for the triggered slow quasistatic rupture to grow into earthquakes.

Triggered creep has also been proposed as a mechanism to explain triggered earthquakes and tremors with some time delay (Shelly *et al.*, 2011). Such a secondary triggering process was observed recently for events following the 2016 M_w 7.8 Kaikōura earthquake (Yao *et al.*, 2021). The experimental observation from this study is generally consistent with these models.

Conclusions

We perform laboratory experiments to investigate near-field dynamic triggering of earthquakes. We provide direct laboratory evidence for the time delay in earthquake triggering, identified as the time required to nucleate the triggered event following the dynamic perturbation. Our results show that the time delay is strongly related to a "disturbed" rupture nucleation process. The physical process governing the near-field dynamic triggering is the evolution of the alteration of the contact state combined with aseismic slip (disturbed nucleation). We also demonstrate that the disturbed rupture nucleation behavior can be predicted using a disturbed nucleation model in combination with the

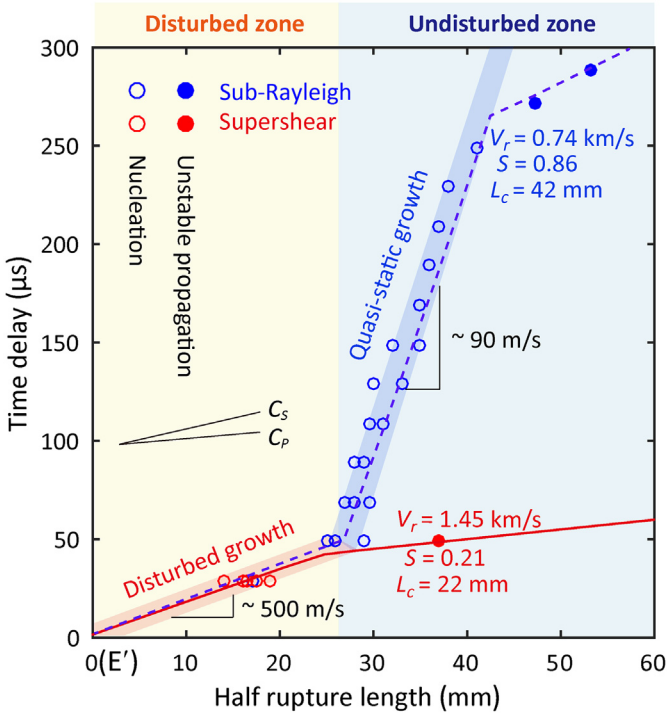

Figure 8. Disturbed nucleation model delineated by rupture fronts during the nucleation. The nucleation process (which depends on the frictional properties of the fault and results from the stress-wave disturbance) is marked by the shaded red strip (corresponding to phase I) and blue strip (corresponding to phase II). Cycles indicate the location of rupture tips for each event at different moments during and after the nucleation. The disturbed and undisturbed zones of the fault are indicated in the figure by light yellow and light blue background shading. The two typical triggered events shown in Figure 3 are highlighted with event parameters and solid lines. The color version of this figure is available only in the electronic edition.

known loading conditions applied to the laboratory fault. This stress state defines a missing slow nucleation phase (II) for faults stressed close to failure (S <0.5) that predictably fail in supershear.

We note that it is difficult to determine the stress (and the failure strength) of real faults. Hence, it is impossible to directly obtain the loading conditions and other key parameters (e.g., the seismic ratio S) to accurately predict the delay time and rupture velocity of triggered events in the field. However, the observed triggering mechanism may provide a possible framework to explain the delayed dynamic triggering from near- through far-field sources by incorporating other relevant physical processes.

Data and Resources

The supplemental material includes two texts (Texts S1–S2) and two figures (Figs. S1 and S2) to better display our experiments and methodology. Data sets for this research are available in Figshare, doi: 10.6084/m9.figshare.13337270.

Declaration of Competing Interests

The authors acknowledge that there are no conflicts of interest recorded.

Acknowledgments

This study was supported by the National Natural Science Foundation of China (Number 42174061), Project funded by China Postdoctoral Science Foundation (Number 2022TQ0319), the Natural Science Foundation of Tianjin (Number 19JCZDJC40400), and the National Key R&D Program of China (Number 2018YFC1503302). R.C. was supported by Open fund for State Key Laboratory of Hydraulic Engineering Simulation and Safety, Tianjin University (Number HESS-1920) and Hunan Provincial Natural Science Foundation of China (Number 2022JJ10058). The authors thank Joan Gomberg from the U.S. Geological Survey (USGS), Chen Ji from UC Santa Barbra, Hiroo Kanamori from Caltech, and John Vidale from USC for discussions. The authors also thank the Editors-in-Chief Allison Bent, editor Annastasia Pratt, and two anonymous reviewers for their constructive comments, which helped to improve the article. Author Contributions: K.X. supervised the study. R.C. and Y.W. conducted the experiments. P.D. and R.C. complied the data and conducted the digital image correlation (DIC) analysis. The article was drafted by P.D. and R.C. and edited by K.X., Z.P., and D.E. All authors contributed to the data interpretation.

References

Andrews, D. J. (1976). Rupture velocity of plane strain shear cracks, *J. Geophys. Res.* **81,** no. 32, 5679–5687.

Andrews, D. J. (1985). Dynamic plane-strain shear rupture with a slip-weakening friction law calculated by a boundary integral method, *Bull. Seismol. Soc. Am.* **75,** no. 1, 1–21.

Antonioli, A., M. E. Belardinelli, A. Bizzarri, and K. S. Vogfjord (2006). Evidence of instantaneous dynamic triggering during the seismic sequence of year 2000 in south Iceland, *J. Geophys. Res.* **111,** no. B3, doi: 10.1029/2005JB003935.

Antonioli, A., M. Cocco, S. Das, and C. Henry (2002). Dynamic stress triggering during the great 25 March 1998 Antarctic plate earthquake, *Bull. Seismol. Soc. Am.* **92,** no. 3, 896–903.

Belardinelli, M. E., M. Cocco, O. Coutant, and F. Cotton (1999). Redistribution of dynamic stress during coseismic ruptures: Evidence for fault interaction and earthquake triggering, *J. Geophys. Res.* **104,** no. B7, 14925–14945.

Ben-David, O., G. Cohen, and J. Fineberg (2010). The dynamics of the onset of frictional slip, *Science* **330,** no. 6001, 211–214.

Blank, D., J. Morgan, and Y. Caniven (2021). Geometrically controlled slow slip enhanced by seismic waves: A mechanism for delayed triggering, *Earth Planet. Sci. Lett.* **554,** 116,695.

Brink, U. T., Y. Wei, W. Fan, J.-L. Granja-Bruña, and N. Miller (2020). Mysterious tsunami in the Caribbean sea following the 2010 Haiti earthquake possibly generated by dynamically triggered early aftershocks, *Earth Planet. Sci. Lett.* **540,** 116,269.

Brodsky, E. E., E. Roeloffs, D. Woodcock, I. Gall, and M. Manga (2003). A mechanism for sustained groundwater pressure changes induced by distant earthquakes, *J. Geophys. Res.* **108,** no. B8, doi: 10.1029/2002JB002321.

Chen, Z., C. Quan, F. Zhu, and X. He (2015). A method to transfer speckle patterns for digital image correlation, *Meas. Sci. Technol.* **26,** no. 9, 095,201.

Das, S. (2007). The need to study speed, *Science* **317,** 905–906.
Dieterich, J. H., and B. Kilgore (1994). Direct observation of frictional contacts: New insights for state-dependent properties, *Pure Appl. Geophys.* **143,** 283–302.
Dunham, E. M. (2007). Conditions governing the occurrence of supershear ruptures under slip-weakening friction, *J. Geophys. Res.* **112,** no. B7, doi: 10.1029/2006JB004717.
Felzer, K. R., and E. E. Brodsky (2006). Decay of aftershock density with distance indicates triggering by dynamic stress, *Nature* **441,** no. 7094, 735–738.
Fossum, A. F., and L. B. Freund (1975). Nonuniformly moving shear crack model of a shallow focus earthquake mechanism, *J. Geophys. Res.* **80,** no. 23, 3343–3347.
Freed, A. M. (2005). Earthquake triggering by static, dynamic, and postseismic stress transfer, *Annu. Rev. Earth Planet. Sci.* **33,** no. 1, 335–367.
Gomberg, J., M. L. Blanpied, and N. M. Beeler (1997). Transient triggering of near and distant earthquake, *Bull. Seismol. Soc. Am.* **87,** no. 2, 294–309.
Gomberg, J., P. Bodin, and P. A. Reasenberg (2003), Observing earthquakes triggered in the near field by dynamic deformations. *Bull. Seismol. Soc. Am.*, **93,** no. 1, 118–138.
Harbord, C. W. A., S. B. Nielsen, N. De Paola, and R. E. Holdsworth (2017). Earthquake nucleation on rough faults, *Geology* **45,** no. 10, 931–934.
Harris, R. A. (1998). Introduction to special section: Stress triggers, stress shadows, and implications for seismic hazard, *J. Geophys. Res.* **103,** no. B10, 24347–24358.
Hill, D. P., and S. G. Prejean (2015). Dynamic triggering, in *Treatise on Geophysics*, Second Ed., G. Schubert (Editor), Elsevier, Oxford, United Kingdom, 273–304.
Hudnut, K. W., L. Seeber, and J. Pacheco (1989). Cross-fault triggering in the November 1987 superstition hills earthquake sequence, southern California, *Geophys. Res. Lett.* **16,** no. 2, 199–202.
Johnson, P. A., and X. Jia (2005). Nonlinear dynamics, granular media and dynamic earthquake triggering, *Nature* **437,** no. 7060, 871–874.
Johnson, P. A., H. Savage, M. Knuth, J. Gomberg, and C. Marone (2008). Effects of acoustic waves on stick-slip in granular media and implications for earthquakes, *Nature* **451,** no. 7174, 57–60.
Kammer, D. S., I. Svetlizky, G. Cohen, and J. Fineberg (2018). The equation of motion for supershear frictional rupture fronts, *Sci. Adv.* **4,** no. 7, eaat5622 , doi: 10.1126/sciadv.aat5622.
Kaneko, Y., S. B. Nielsen, and B. M. Carpenter (2016). The onset of laboratory earthquakes explained by nucleating rupture on a rate-and-state fault, *J. Geophys. Res.* **121,** no. 8, 6071–6091.
Kato, N., K. Yamamoto, H. Yamamoto, and T. Hirasawa (1992). Strain-rate effect on frictional strength and the slip nucleation process, *Tectonophysics* **211,** 269–282.
Kilb, D., J. Gomberg, and P. Bodin (2000). Triggering of earthquake aftershocks by dynamic stresses, *Nature* **408,** 570–574.
Latour, S., A. Schubnel, S. Nielsen, R. Madariaga, and S. Vinciguerra (2013). Characterization of nucleation during laboratory earthquakes, *Geophys. Res. Lett.* **40,** no. 19, 5064–5069.
Liu, C., A. Bizzarri, and S. Das (2014). Progression of spontaneous in-plane shear faults from sub-Rayleigh to compressional wave rupture speeds, *J. Geophys. Res.* **119,** no. 11, 8331–8345.
McLaskey, G. C. (2019). Earthquake initiation from laboratory observations and implications for foreshocks, *J. Geophys. Res.* **124,** no. 12, 12,882–12,904.
Nielsen, S., J. Taddeucci, and S. Vinciguerra (2010). Experimental observation of stick-slip instability fronts, *Geophys. J. Int.* **180,** no. 2, 697–702.
Nissen, E., J. R. Elliott, R. A. Sloan, T. J. Craig, G. J. Funning, A. Hutko, B. E. Parsons, and T. J. Wright (2016). Limitations of rupture forecasting exposed by instantaneously triggered earthquake doublet, *Nature Geosci.* **9,** no. 4, 330–336.
Ohnaka, M. (1996). Nonuniformity of the constitutive law parameters for shear rupture and quasistatic nucleation to dynamic rupture: A physical model of earthquake generation processes, *Proc. Natl. Acad. Sci. Unit. States Am.* **93,** 3795–3802.
Ohnaka, M. (2003). A constitutive scaling law and a unified comprehension for frictional slip failure, shear fracture of intact rock, and earthquake rupture, *J. Geophys. Res.* **108,** no. B2, doi: 10.1029/2000JB000123.
Ohnaka, M., and Y. Kuwahara (1990). Characteristic features of local breakdown near a crack-tip in the transition zone from nucleation to unstable rupture during stick-slip shear failure, *Tectonophysics* **175,** no. 1, 197–220.
Ozacar, A. A., and S. L. Beck (2004). The 2002 Denali fault and 2001 Kunlun fault earthquakes: Complex rupture processes of two large strike-slip events, *Bull. Seismol. Soc. Am.* **94,** no. 6, S278–S292.
Ozacar, A. A., S. L. Beck, and D. H. Christensen (2003). Source process of the 3 November 2002 Denali fault earthquake (central Alaska) from teleseismic observations, *Geophys. Res. Lett.* **30,** no. 12, 1638.
Palmer, A. C., and J. R. Rice (1973). Growth of slip surfaces in progressive failure of over- consolidated clay, *Proc. Math. Phys. Eng. Sci.* **332,** no. 1591, 527–548.
Parsons, T. (2005). A hypothesis for delayed dynamic earthquake triggering, *Geophys. Res. Lett.* **32,** no. 4, L04302, doi: 10.1029/2004GL021811.
Passelègue, F. X., A. Schubnel, S. Nielsen, H. S. Bhat, and R. Madariaga (2013). From sub-Rayleigh to supershear ruptures during stick-slip experiments on crustal rocks, *Science* **340,** no. 6137, 1208–1211.
Perfettini, H., J. Schmittbuhl, and A. Cochard (2003). Shear and normal load perturbations on a two-dimensional continuous fault: 2. Dynamic triggering, *J. Geophys. Res.* **108,** no. B9, 2409.
Richards-Dinger, K., R. S. Stein, and S. Toda (2010). Decay of aftershock density with distance does not indicate triggering by dynamic stress, *Nature* **467,** no. 7315, 583–586.
Rubino, V., A. J. Rosakis, and N. Lapusta (2017). Understanding dynamic friction through spontaneously evolving laboratory earthquakes, *Nat. Commun.* **8,** 15,991.
Rubino, V., A. J. Rosakis, and N. Lapusta (2019). Full-field ultrahigh-speed quantification of dynamic shear ruptures using digital image correlation, *Exp. Mech.* **59,** 551–582.
Rubino, V., A. J. Rosakis, and N. Lapusta (2020). Spatiotemporal properties of sub-Rayleigh and supershear ruptures inferred from full-field dynamic imaging of laboratory experiments, *J. Geophys. Res.* **125,** no. 2, e2019JB018922, doi: 10.1029/2019JB018922.
Rubinstein, S. M., G. Cohen, and J. Fineberg (2004). Detachment fronts and the onset of dynamic friction, *Nature* **430,** no. 7003, 1005–1009.
Rubinstein, S. M., G. Cohen, and J. Fineberg (2007). Dynamics of precursors to frictional sliding, *Phys. Rev. Lett.* **98,** no. 22, 226,103.

Scholz, C. H. (1988). The critical slip distance for seismic faulting, *Nature* **336,** no. 6201, 761–763.

Shelly, D. R., Z. Peng, D. P. Hill, and C. Aiken (2011). Triggered creep as a possible mechanism for delayed dynamic triggering of tremor and earthquakes, *Nature Geosci.* **4,** no. 6, 384–388.

Svetlizky, I., G. Albertini, G. Cohen, D. S. Kammer, and J. Fineberg (2020). Dynamic fields at the tip of sub-Rayleigh and supershear frictional rupture fronts, *J. Mech. Phys. Solids* **137,** 103,826.

Svetlizky, I., D. S. Kammer, E. Bayart, G. Cohen, and J. Fineberg (2017). Brittle fracture theory predicts the equation of motion of frictional rupture fronts, *Phys. Rev. Lett.* **118,** no. 12, 125,501.

Tal, Y., V. Rubino, A. J. Rosakis, and N. Lapusta (2022). Dynamics and near-field surface motions of transitioned supershear laboratory earthquakes in thrust faults, *J. Geophys. Res.* **127,** no. 3, e2021JB023733, doi: 10.1029/2021JB023733.

van der Elst, N. J., and E. E. Brodsky (2010). Connecting near-field and far-field earthquake triggering to dynamic strain, *J. Geophys. Res.* **115,** no. B7, doi: 10.1029/2009JB006681.

van der Elst, N. J., and H. M. Savage (2015). Frequency dependence of delayed and instantaneous triggering on laboratory and simulated faults governed by rate-state friction, *J. Geophys. Res.* **120,** no. 5, 3406–3429.

Venkataraman, A., and H. Kanamori (2004). Observational constraints on the fracture energy of subduction zone earthquakes, *J. Geophys. Res.* **109,** no. B5, doi: 10.1029/2003JB002549.

West, M., J. J. Sánchez, and S. R. McNutt (2005). Periodically triggered seismicity at Mount Wrangell, Alaska, after the Sumatra earthquake, *Science* **308,** no. 5725, 1144–1146.

Xia, K., A. J. Rosakis, and H. Kanamori (2004). Laboratory earthquakes: The sub-Rayleigh-to-supershear rupture transition, *Science* **303,** no. 5665, 1859–1861.

Xia, K., A. J. Rosakis, H. Kanamori, and J. Rice (2005). Laboratory earthquakes along inhomogeneous faults: Directionality and supershear, *Science* **308,** no. 5722, 681–684.

Yao, D., Z. Peng, Y. Kaneko, B. Fry, and X. Meng (2021). Dynamic triggering of earthquakes in the North Island of New Zealand following the 2016 Mw 7.8 Kaikōura earthquake, *Earth Planet. Sci. Lett.* **557,** 116,723.

Zhuo, Y.-Q., P. Liu, S. Chen, Y. Guo, and J. Ma (2018). Laboratory observations of tremor-like events generated during preslip, *Geophys. Res. Lett.* **45,** no. 14, 6926–6934.

Manuscript received 16 August 2022
Published online 18 November 2022